WILEY

RESEARCH ARTICLE

Evaluation of different wind fields for the investigation of the dynamic response of offshore wind turbines

Astrid Nybø[1] | Finn Gunnar Nielsen[1] | Joachim Reuder[1] | Matthew J. Churchfield[2] | Marte Godvik[1,3]

[1]Geophysical Institute and Bergen Offshore Wind Centre (BOW), University of Bergen, Bergen, Norway

[2]National Wind Technology Center, National Renewable Energy Laboratory, Boulder, Colorado, USA

[3]Equinor, Bergen, Norway

Correspondence
Astrid Nybø, Geophysical Institute and Bergen Offshore Wind Centre (BOW), University of Bergen, Allégaten 70, 5007 Bergen, Norway.
astrid.nybo@uib.no

Abstract

As the size of offshore wind turbines increases, a realistic representation of the spatiotemporal distribution of the incident wind field becomes crucial for modeling the dynamic response of the turbine. The International Electrotechnical Commission (IEC) standard for wind turbine design recommends two turbulence models for simulations of the incident wind field, the Mann spectral tensor model, and the Kaimal spectral and exponential coherence model. In particular, for floating wind turbines, these standard models are challenged by more sophisticated ones. The characteristics of the wind field depend on the stability conditions of the atmosphere, which neither of the standard turbulence models account for. The spatial and temporal distribution of the turbulence, represented by coherence, is not modeled consistently by the two standard models. In this study, the Mann spectral tensor model and the Kaimal spectral and exponential coherence model are compared with wind fields constructed from offshore measurements and obtained from large-eddy simulations. Cross sections and durations relevant for offshore wind turbine design are considered. Coherent structures from the different simulators are studied across various stability conditions and wind speeds through coherence and proper orthogonal decomposition mode plots. As expected, the standard models represent neutral stratification better than they do stable and unstable. Depending upon the method used for generating the wind field, significant differences in the spatial and temporal distribution of coherence are found. Consequently, the computed structural design loads on a wind turbine are expected to vary significantly depending upon the employed turbulence model. The knowledge gained in this study will be used in future studies to quantify the effect of various turbulence models on the dynamic response of large offshore wind turbines.

KEYWORDS

coherence, offshore wind turbines, proper orthogonal decomposition mode, turbulence models, wind fields

1 | INTRODUCTION

The current standards of offshore wind turbine modeling recommend the use of a rather simple turbulence model to represent the wind characteristics.[1-3] These models are based upon knowledge of wind over land, small turbines, and fixed foundations. As the rotor size of offshore wind turbines becomes increasingly large,[4] the variation of the wind in time and space over the rotor diameter becomes increasingly important. For large, bottom-fixed, offshore wind turbines, the lowest relevant frequency for load analysis is the nominal rotor frequency of about 10 revolutions per minute. Moving towards floating wind turbines, one has to additionally account for the natural modes related to the rigid body motions. Depending upon the design, natural periods for the six rigid body modes of motion may range from a few seconds to at least 100 s.

These low-frequency natural periods represent new challenges to the description of the wind field. Both the turbulent energy at low frequencies and the spatial structure of the turbulence must be realistic to obtain realistic loads.

Either the Mann spectral tensor model,[5] hereafter denoted "Mann," or the Kaimal[6] spectral and exponential coherence model,[1] hereafter denoted "Kaimal," is recommended by the International Electrotechnical Commission (IEC) wind turbine design standard.[1] Several studies have shown that the response of a wind turbine is dependent on the turbulence model chosen.[7-10] The difference is predominant at low frequencies,[7,10] as mentioned, interesting for floating wind turbines. Based on this experience, it is highly relevant to evaluate the ability of the two turbulence models, Kaimal and Mann, to represent an offshore wind field.

Point statistics, such as wind speed and turbulence intensity (TI) at hub height, have great impact on the response of a wind turbine (e.g., Robertson et al.[11]). However, for larger rotors where the spatial and temporal distribution of the wind field is increasingly important, wind shear and coherent structures play an increasingly important role. The wind shear represents the variation of mean wind speed over the rotor height. The presence of coherent structures may be illustrated temporally by the coherence at a certain separation distance over various frequencies. Coherence is commonly referred to as correlation in frequency space.[12] Spatially, coherent structures may be identified by proper orthogonal decomposition over the rotor plane, hereafter denoted "POD."

The two simple turbulence models recommended by the standard generate wind fields with equal point statistics and shear. The coherence and POD modes are, however, dependent on the model chosen.[7,9,13,14] Previous studies by Eliassen and Ohbrai, Cheynet, and Cheynet et al. have compared turbulence models with offshore measurements, with a special focus on spectra and coherence.[13,15,16] They all use measurements from the offshore mast, FINO1, located in the North Sea.[17] Measurements from offshore masts provide crucial understanding of the offshore wind field. This is very valuable when evaluating wind field models. However, measurements should not necessarily be considered as the "truth." They are only made at a few spatial points and require proper processing and quality assurance. One may simulate offshore wind fields based on point measurements, using, for example, the TIMESR function in the turbulence simulator TurbSim,[18] but this requires several assumptions and simplifications.

Large-eddy simulations, hereafter denoted "LES," provide a more advanced method for generating the wind field based upon physical principles. It is based on solving momentum and pressure equations, requiring significant computational effort. Previous studies by, for example, Doubrawa et al.,[9] Simley and Pao,[19] Worsnop et al.,[20] and Berg et al.[21] compared the wind fields of Kaimal and/or Mann with LES. In contrast to comparisons with point measurements, this enables evaluations of, for example, lateral coherence and POD modes.

The turbulence models recommended by the IEC design standard are originally intended for neutral stratification.[1] The standard allows for an adaptation of turbulence intensity to non-neutral conditions. However, the other standard parameters are constant regardless of atmospheric stability conditions. It is shown by Sathe and Bierboms,[22] Eliassen et al.,[23] Holtslag et al.,[24,25] Doubrawa et al.,[9] and Sathe et al.[26] that the atmospheric stability influences the wind profile and turbulent structure of the wind field and therefore also the dynamic response of wind turbines. It is therefore relevant to evaluate the standard models also towards measurements or LES of other atmospheric stability conditions. This is especially interesting offshore, where the ambient turbulence is lower. This leads to a longer wake recovery, greatly dependent on stability conditions.

The current study evaluates the turbulence models recommended by the IEC design standard, Mann and Kaimal, from both a meteorological and wind turbine response point of view. The evaluation includes a comparison of the standard wind fields with offshore measurements and LES. Both processed raw data and wind fields created from these point measurements are used in the comparisons. The LES are run using the simulation tool SOWFA.[27] The study includes a description of the standard turbulence models and how they are used in industry. They are evaluated in different atmospheric stability conditions and at different wind speeds. The Kaimal and Mann spectral formulations both inherently assume neutral flow. In the present work, when it is referred to stable or unstable conditions for these spectral formulations, only the turbulence intensity and wind profile have been fitted to the flow conditions considered. In total, nine simulations are performed for each simulation method, covering below, close to, and above rated wind speed in unstable, neutral, and stable atmospheric conditions. We aim to highlight spatial and temporal differences in wind fields from various simulators across various atmospheric stability conditions. We will focus on differences that may play an important role for the dynamic response of large offshore wind turbines. These are illustrated through coherence and POD modes. Further work will use the various generated wind fields in dynamic response analysis, which will give further insight in the capabilities of the two standard turbulence models. Wind field simulations of slightly more than 1 h in duration are performed for this reason. Within 1 h, all relevant frequencies of large, bottom-fixed, and floating wind turbines are resolved and sufficiently represented. A total of 200 additional seconds are added in order to account for ramp up of the loads in modelling. The DTU 10-MW reference turbine will be used as reference where relevant.[28] This turbine has a diameter of 178.3 m, a hub height of 119 m, and a rated wind speed of 11.4 m/s.

The following section provides information on the methods used in the wind field analysis and explains the standard turbulence models, the measurements, and the LES, in addition to describing the details on the simulation of the different situations. Thereafter follows an overview of the generated wind fields and a comparison of the turbulent structures observed across simulation methods and atmospheric stability conditions. Last, conclusions are drawn on the basis of these results.

2 | DATA AND METHODS

2.1 | Wind field analysis

2.1.1 | Point statistics

The mean wind speed and the turbulence intensity at hub height have large impact on the response of wind turbines. For comparisons of wind field characteristics from different wind field simulators, we strive to achieve similar values for these statistical parameters. Following this approach, we exclude the dominating effects of those bulk parameters on the dynamic response of wind turbines. This enables us to focus on differences related to the turbulent flow characteristics created by the different simulators, such as coherence and stability dependence of turbulent structures.

The turbulence intensity is defined as the standard deviation of the wind speed in the mean wind direction, σ_u, divided by the mean wind speed, $\bar{u}$. In wind energy-related meteorology, the turbulence intensity is commonly calculated from 1-Hz measurements, the typical temporal resolution of cup anemometers, averaged over 10 min. This frequency range is of high importance for wind turbine response. Sim et. al[29], among others, showed that the high-frequency region has less impact on the response. For floating wind turbines, the low-frequency region is of higher importance, but all relevant frequencies are resolved within a 10-min averaging interval.

2.1.2 | Wind profile

In wind industry, either the power law or the logarithmic law are commonly used to formulate wind profiles.[1] Knowing the wind speed at one height and a few characterizing parameters of the atmosphere, the wind speed at a desired height is given by the mentioned relations.

The power law, the simplest of the two mentioned relations, is given by

$$\bar{u}(z) = \bar{u}_{ref} \left(\frac{z}{z_{ref}} \right)^{\alpha}, \tag{1}$$

where $\bar{u}$ is the mean wind speed at the actual height, $\bar{u}_{ref}$ is the wind speed at the reference height, z is the actual height, z_{ref} is the reference height, and α is the empirical power law exponent. The IEC design standard[1] defines the normal wind speed profile for the standard wind turbine classes to be given by the power law. The alpha exponent can be interpreted as a bulk parameter including the effects of surface roughness (expressed by the roughness length, z_0), and atmospheric stability.[30,31] The relative contribution of the two is, however, not easily distinguishable, particularly for offshore conditions where the surface roughness is variable, mainly depending on the wave height.

In contrast, the extended form of the logarithmic wind profile typically used in boundary layer meteorology allows for a separation between roughness and stability effects. The effect of atmospheric stability is here included by the introduction of a stability correction function, ψ.[32] However, in the wind industry,[1] this parameter is often excluded, thus assuming a neutral atmosphere. The logarithmic law is given by

$$\bar{u}(z) = \bar{u}_{ref} \left(\frac{\ln\left(\frac{z}{z_0}\right) - \psi}{\ln\left(\frac{z_{ref}}{z_0}\right) - \psi} \right). \tag{2}$$

The numerical coefficients in the stability function, ψ, vary slightly in the literature.[33] In TurbSim, the following formulation is used[18]:

$$\psi = \begin{cases} 0, & \text{when neutral,} \\ -5\zeta, & \text{when stable,} \\ 2\ln\frac{1+x}{2} + \ln\frac{1+x^2}{2} - 2\tan^{-1}(x) + \frac{\pi}{2}, & \text{when unstable,} \end{cases} \tag{3}$$

where $x = (1 - 15\zeta)^{1/4}$. The stability parameter, ζ, is defined in Section 2.1.3. The constants involved in this formulation (5 in stable conditions and 15 in the expression for x in unstable conditions) are in accordance with Dyer[34] and Businger et al.,[32] respectively.

The applicability of the logarithmic wind profile is limited to situations of at least moderate winds and a corresponding clearly nonzero friction velocity, but this is, in general, no issue for the wind speed range of wind turbine power production. Another more relevant limitation is arising from the fact that the logarithmic wind profile and the stability corrections are based on the theoretical framework of the Monin–Obukhov similarity theory (MOST).[35,36] MOST originated from and is validated by measurements over homogeneous land surfaces[37,38] and thus might not be fully representative of offshore conditions. In addition, it is limited to the so-called surface layer, where the turbulent fluxes are assumed to be constant with height. The surface layer roughly covers 10 % of the atmospheric boundary layer[39] and thus typically extends vertically over about 100 m for unstable and considerably less (in the order of a few tenths of meters) for stable conditions. Those limitations apply in general also to the power law formulation, and the appropriate characterization of wind profiles over the whole rotor disk of state-of-the-art wind turbines is therefore still a challenge,[40] particularly offshore. [41]

TABLE 1 Stability classification after van Wijk et al.[43]

Stability	Range
Very stable	0<L<200 m
Stable	200<L<1000 m
Near neutral	|L| >1000 m
Unstable	-1000<L<-200 m
Very unstable	-200<L<0 m

2.1.3 | Stability classification

Considering the loading on a horizontal axis wind turbine, the blades will experience dynamic loads both due to wind shear and the turbulence characteristics of the inflow. The relative importance of these contributions will depend upon the stability condition. The Obukhov length, L, is a parameter commonly used for classifying atmospheric stability in the surface layer.[42] It expresses the ratio between shear effects and buoyancy effects in the production of turbulence. The Obukhov length is proportional to the vertical distance above the surface where the buoyancy effect dominate over the shear effects. Its formulation is given accordingly:

$$L = \frac{-\overline{\theta_v} u_*^3}{kg\left(\overline{w'\theta'}\right)_s},$$ (4)

where $\overline{\theta_v}$ is the virtual potential temperature, u_* is the friction velocity defined by Equation (5), k is the von Karman constant, g is the gravitational constant, $\left(\overline{w'\theta'}\right)_s$ is the surface vertical kinematic eddy heat flux, and u', v', and w' are the longitudinal, lateral, and vertical velocity fluctuations, respectively.

$$u_*^2 = \sqrt{\overline{u'w'}^2 + \overline{v'w'}^2}$$ (5)

Table 1 shows the stability classification based on Obukhov length ranges from van Wijk et al.[43] This classification gives a wide range of stable and unstable Obukhov lengths. Gryning et al. propose alternative classification intervals, where $|L|>200$ is already considered near neutral.[40]

ζ is a nondimensional parameter, providing information on the stability of the atmosphere, given by the Obukhov length, and the height above the surface, z:

$$\zeta = \frac{z}{L}.$$ (6)

2.1.4 | Spectral analysis

The wind spectrum provides information of the power spectral density and is computed by a Fourier transform of the corresponding time series. In order to represent the time series, stationary conditions must be assumed. Most energy is located in the low-frequency region where turbulent energy is created, for example, by convection or vertical shear in the mean flow. This frequency range is also very relevant for offshore wind turbine response.[10] At midfrequencies is the inertial subrange characterized by the Kolmogorov slope of -5/3 ($S(f) \propto f^{(-5/3)}$), whereas turbulence dissipation happens at the highest frequencies. High-frequency sonic anemometer measurements typically resolve a considerable portion of the inertial subrange. The simple wind field simulators of this study are able to reproduce an energy spectrum similar to the measurements given a similar turbulence intensity level. The LES, on the other hand, is not able to reproduce the higher frequency region of the inertial subrange without substantial computational costs. The amount of high-frequency energy lost is dependent on both the temporal and spatial resolution[29]; fractal interpolation may enhance the energy level of the high-frequency region of the spectrum. The low-frequency region is, however, more important for the dynamic response of offshore wind turbines, so fractal interpolation or other techniques to enhance the energy in the higher frequency region are not considered in this study. The spectra of this study are estimated using Welch's algorithm[44] with a Hamming window, six segments, and 50 % overlapping. Detrended 60-min periods are used for the estimations.

Even though the simple turbulence models are able to achieve a similar energy spectrum at hub height, the spatial characteristics differ between the models. This may be represented by the coherence, which describes the correlation between two time series sampled at a given separation distance. The coherence is a function of the period of the fluctuations in the wind velocities and is thus conveniently described in the frequency domain. Coherence may be expressed as follows:

$$\gamma = \frac{|S_{xy}|}{\sqrt{S_{xx}S_{yy}}},$$ (7)

where S_{xx} and S_{yy} are one-sided auto-spectra of the wind velocities at two different positions, x and y, and S_{xy} is the cross spectrum between these two. Equation (7) expresses the coherence in its absolute form, the root coherence. It may also be split in a real part, the co-coherence, and an imaginary part, the quad coherence. In engineering applications, the quad coherence is often ignored as it is assumed far less significant than the co-coherence. This has been the traditional approach in the wind energy industry. Veers[45] showed how the generation of a turbulent wind field for numerical analysis was simplified by ignoring the quad coherence, assuming that the wind velocity fluctuations are in phase. For Veers, in studying a 17-m diameter rotor, this was a reasonable assumption. However, the assumption can be questioned for state-of-the-art rotor diameters, now exceeding 200 m.

2.1.5 | Proper orthogonal decomposition

POD modes illustrate coherent structures or events in turbulent flows, as shown by Eliassen and Andersen [14] and Bachynski and Eliassen,[7] for example. In particular, the lowest modes, which explain the majority of the variation of the wind fields, are interesting for offshore wind turbines. These modes are the most anisotropic and are related to the large coherent structures found in the low-frequency part of the energy spectrum. In this study, only the POD modes of the longitudinal velocity component are considered. The POD modes, $\mathbf{\Phi}$, as formulated by Jørgensen et al.,[46] are defined by the matrices of eigenvectors, $\mathbf{G}$, eigenvalues, Λ, and the turbulent part of the wind field, $\mathbf{U}$:

$$\mathbf{\Phi} = \mathbf{U}\mathbf{G}\Lambda^{-1/2}, \tag{8}$$

where the matrix of orthonormal eigenvectors are defined as

$$\mathbf{G} = \begin{bmatrix} \mathbf{g_1} & \cdots & \mathbf{g_{n-1}} \end{bmatrix}, \tag{9}$$

the matrix of eigenvalues in decreasing order as

$$\Lambda = \begin{bmatrix} \lambda_1 & & 0 \\ & \ddots & \\ 0 & & \lambda_{n-1} \end{bmatrix}, \tag{10}$$

and the velocity matrix divided into time/space slices as

$$\mathbf{U} = \begin{bmatrix} \mathbf{u'_1} & \cdots & \mathbf{u'_n} \end{bmatrix}. \tag{11}$$

The eigenvalue problem is represented by the following equation:

$$\mathbf{R}\mathbf{G} = \mathbf{G}\Lambda, \tag{12}$$

where the auto-covariance matrix is defined as $\mathbf{R} = \mathbf{U}^{\mathsf{T}}\mathbf{U}$.

The wind field may be reconstructed by the POD modes from rearranging Equation (8):

$$\mathbf{U} = \mathbf{\Phi}\mathbf{G}^{\mathsf{T}}\Lambda^{1/2}. \tag{13}$$

The least energetic POD modes may be excluded in the reconstruction, without significant loss of accuracy. The results of this study present the four most energetic POD modes and the amount of variation explained by these modes (eigenvalues) of various wind fields. For details of POD for turbulent flows, see Berkooz, Holmes, and Lumley.[47]

2.2 | Standard turbulence models

Both turbulence models recommended by the IEC wind turbine design standard,[1] the Mann uniform shear model (Mann) and the Kaimal spectrum and exponential coherence model (Kaimal), are stationary models, intended for neutral atmospheric conditions in the surface layer. The input parameters of the models are also suggested by the standards, being equal onshore and offshore.[1-3] The wind fields generated by the Mann and Kaimal models in the following use these standard inputs. The only exceptions are the turbulence intensities and wind profiles. These are fitted to the measurements for each stability condition and wind speed.

2.2.1 | The Mann uniform shear model

The Mann uniform shear model,[5,48] introduced in 1994, is a spectral tensor model based on von Karman's model[49] but assumes that the isotropic energy spectrum is rapidly distorted by a uniform mean velocity shear. It is emphasized by Mann[50] that the assumption of linear shear is not valid at low frequencies related to large eddies, and homogeneity is not valid for large vertical separations. The root coherence of Mann is given by the integral of the spectral tensor, ϕ, and is commonly formulated as

$$\gamma = \frac{|\iint \phi_{ij}(\mathbf{k})exp(-ik_y\delta_y)exp(-ik_z\delta_z)dk_ydk_z|}{\sqrt{\iint \phi_{ii}(\mathbf{k})dk_ydk_z\phi_{jj}(\mathbf{k})dk_ydk_z}}, \tag{14}$$

where i and $j = 1, 2, 3$ for the longitudinal, lateral, and vertical turbulent wind components, $\mathbf{k}$ is the wave vector, k_y the wave number in the lateral direction, k_z the wave number in the vertical direction, δ_y the separation distance in the lateral direction, and δ_z the separation distance in the vertical direction. The root coherence is originally formulated by the wave spectrum, but may be transformed to frequency notation by the relation $f = \frac{k\bar{u}}{2\pi}$.

The Mann model is based on three parameters: $\alpha\epsilon^{2/3}$, the Kolmogorov constant multiplied with the rate of the viscous dissipation of specific turbulent kinetic energy to the two thirds, l, the length scale, and Γ, the nondimensional parameter related to the lifetime of the eddies. The

parameters suggested by the IEC standard are used,[1] with the exception of the turbulence intensity included in the determination of $\alpha \epsilon^{2/3}$, which is taken from measurements. The standard parameters are constant, even though several studies show that they are a function of atmospheric stability.[26,51,52]

The DTU Mann generator[53] is used to generate wind fields from the Mann model. A three-dimensional box of $32768 \times 64 \times 64$ nodes and grid size of 3.5 m in vertical and lateral directions are used for the simulations. In the main wind direction, the grid size varies with the mean wind velocity. In the present cases, the range is from 0.9 to 2.1 m. Assuming the validity of Taylor's hypothesis of "frozen" turbulence, this corresponds to 1 h and 200 s of simulation, through the relationship $\bar{u}T/N_x$, where $\bar{u}$ is the mean wind speed, T is the total time, and N_x is the number of grid points in the longitudinal direction. Additional 200 s are included to allow for transient effects to die out in future dynamic simulations of wind turbines and thus achieve 1 h of almost stationary response. The corresponding time step is 0.116 s.

2.2.2 | The Kaimal spectrum and exponential coherence model

The other model recommended by the IEC is the Kaimal spectrum and exponential coherence model. [1,6] A two-parameter exponential coherence model for the wind velocity in the mean wind direction is used. Unlike the Mann model, no coherence is modeled for the lateral and vertical velocity components. The coherence for the velocity in the mean wind direction is given as

$$\gamma = \exp\left(-12\left((f\delta/\bar{u}_{hub})^2 + (0.12\delta/L_c)^2\right)^{0.5}\right),$$ (15)

where f is the frequency, δ the magnitude of the separation distance on a plane normal to the mean wind direction, $\bar{u}_{hub}$ the wind speed at hub height, and L_c the coherence scale parameter, defined as $8.1\Lambda_1$, where Λ_1 is the turbulence scale parameter in meters. According to this equation, the coherence is real and positive. This implies that all along-wind velocity variations over the cross section are in phase. Considering state-of-the-art rotor sizes, this is a doubtful assumption. Particularly in the vertical direction, significant phase shifts may be encountered. This issue will be addressed in the following.

A turbulence simulator from the National Renewable Energy Laboratory (NREL), TurbSim, [18] is used to compute the wind fields using the Kaimal model. In general, TurbSim creates turbulent wind fields from a chosen spectral model together with a chosen spatial coherence model. The shear profile is not accounted for in the turbulence generation but is added to the wind field afterwards. The software is commonly used to simulate wind fields with the Kaimal spectra and exponential coherence model defined by the IEC design standard.[1] The same grid resolution as for the Mann model is used in the lateral and vertical directions. Assuming Taylor's hypothesis of the Mann wind box, the temporal resolution is also approximately equal.

2.3 | Measurements

2.3.1 | FINO-1

The offshore measurements used in this study are obtained from the German research platform FINO-1, located in the North Sea north of Borkum.[17] The platform is equipped with a meteorological mast with sonic anemometers located at 40, 60, and 80 m above sea level. Both wind speed and sonic temperature measurements are available at 10–20 Hz from these anemometers. Data from the period June 2015 to September 2016 are considered. These data have been thoroughly quality controlled as described by Nybø et al.[54] In the present work, samples of the data have been investigated further and used as input to TurbSim to create realistic 3D wind fields. These wind fields are subsequently compared with wind fields obtained by using standard turbulence models.

2.3.2 | Processing measurement data

A processing procedure is applied to the measurements from the sonic anemometers in Nybø et al.,[54] resulting in a thoroughly quality assured data set of more than 6000 30-min periods. A conservative approach is followed, limiting the final availability to only 27 %. Data are unavailable or removed due to the following:

- instrument downtime,
- issues with the data logger,
- rain as the sonic anemometers give erroneous data during and following rain,
- other disturbances detected by high temperature standard deviation,
- mast shadow, nearby wind parks, and nearby land assuming only wind coming from north–west is undisturbed, and
- organizing data of 10 min into blocks of data of 30 min duration.

The impact of each of these steps on the overall availability is shown in Table 2. Additionally, a spike detection and removal procedure based on Rinker et. al[55] removes a few extreme samples. We assume that all relevant frequencies are resolved within 30 min. However, when 1-h periods with desired characteristics are available, these are used for wind turbine simulations.

Total number of periods	Missing	Corrupted	Rainy	High σ_T	Shadow	30 min	Processed
100 %	11.8 %	0.6 %	16.2 %	13.2 %	27.7 %	3.8 %	26.7 %
23 424 periods							6 252 periods

TABLE 2 Total number of 30-min periods from June 2015 to September 2016, fractions of removed data at all heights relevant to the total number of periods, and net remaining availability after processing of the sonic anemometer data at all heights in the last column
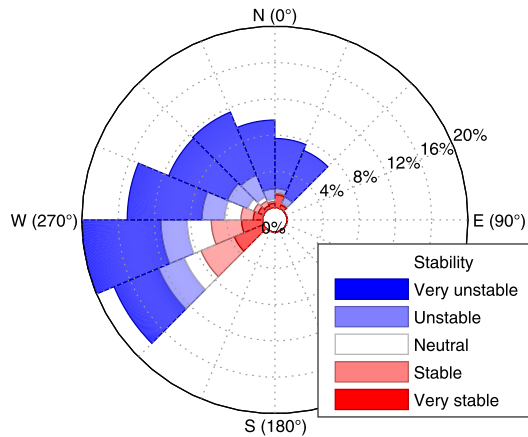
FIGURE 1 Distribution of stability (at 40 m) as function of wind direction for 30-min periods of measurements at FINO1 [Colour figure can be viewed at wileyonlinelibrary.com]
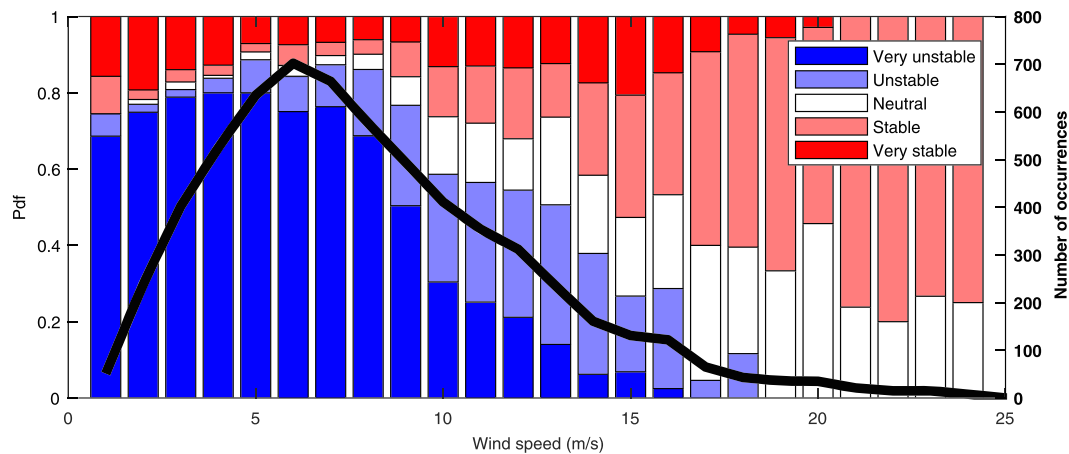
FIGURE 2 Distribution of stability (at 40 m) as function of wind speed (at 80 m) for 30-min periods of measurements at FINO1. Solid line corresponding to the right axis represents the number of occurrences within each wind speed interval of 1 m/s [Colour figure can be viewed at wileyonlinelibrary.com]

2.3.3 | Characteristics at FINO-1 in given period

An overview of the wind speed, turbulence intensity, and direction of the processed data set is shown in Nybø et al.[54] The mean wind speed of the available periods is 8.1 m/s at 80 m above sea level. In the measured data, there is a wide range of turbulence intensities at low wind speeds. At higher wind speeds, the TI is typically in the range of 5 % to 10 %.

Figure 1 shows the distribution of stability classes as function of wind direction. After removing periods where the wind speed originates from the disturbed sector, we see that the most frequent wind direction is westerly. Higher wind speeds and neutral to stable conditions are more frequent in the western wind. As explained by Cheynet et al.,[16] the wind from southwest is typically stable due to the proximity of land and the corresponding transport of warm air over shorter fetches over sea, particularly during summer. Wind from northwest is more frequently associated with unstable conditions, caused by cold air advection over relatively warm sea, especially in the winter season.

With increasing wind speed, one expects more frequent neutral atmospheric stability. This relation is confirmed by the FINO1 measurements presented in Figure 2. Offshore, we still expect variations in atmospheric stability to exist even at high wind speeds. This is related to the low friction of the water surface, represented by the friction velocity in the Obukhov length calculation (Equation 4), causing stable conditions. Unstable conditions are generally less frequent offshore, but consistently with the findings of Cheynet et al.[16] and Krogsæter and Reuder,[56] Figure 2 shows that unstable situations are common at low wind speeds at FINO1.

2.3.4 | Generating realistic offshore wind fields from sonic measurements at different heights

An alpha version of the turbulence simulator TurbSim[18] is used to create wind fields based on specific measured situations. As mentioned earlier, this software is commonly used to simulate wind fields according to the IEC wind turbine design standard. Another option is to provide time series of measurements as inputs (TIMESR), used by, for example, Shaler et al.[57] With this option, TurbSim calculates the spectral amplitudes of

TABLE 3 Decay coefficients from measurements used as inputs in TurbSim

Wind speed (m/s)	Stability	C_u	C_v	C_w
7.5	Unstable	9.4	6.0	3.6
7.5	Neutral	13.8	6.6	3.8
7.5	Stable	28.5	24.0	21.6
12.5	Unstable	12.9	7.7	4.9
12.5	Neutral	12.5	8.1	4.7
12.5	Stable	52.5	42.2	31.0
18	Unstable	12.6	8.6	5.3
18	Neutral	11.9	7.7	6.3
18	Stable	68.9	29.6	29.7

the input time series. The spectral amplitudes of all simulated grid points in a yz plane are given by linear interpolation of the spectra of the input time series or "nearest neighbor" extrapolation. Input time series from the sonic anemometers at 40, 60, and 80 m above mean sea level are used with a sampling frequency of 10 Hz. Initially, TurbSim uses Veer's method[45] to generate random phases (dependent on seed) at each simulated point. Thereafter, the phases are modified using a coherence function and a recursive procedure, ensuring proper coherence between all points. In TIMESR, the phases are subsequently shifted so that the input time series of a reference point is reproduced in the output wind field.

The measured wind speed at 80 m above the surface is used as reference. This height is chosen due to its proximity to the hub height, assuming that the phase information at this height is more important for the rotor wind field. The Davenport coherence model is used to ensure coherence between the 80-m data and simulated points. The coherence of the three wind components, $K = u, v, w$, for two points in space, i and j, is given by Equation (16) according to the Davenport model:

$$\gamma_{i,jK} = \exp\left(-C * \frac{f\delta}{\bar{u}_m}\right),$$ (16)

where C is the decay coefficient, f is the frequency of measurements, δ is the separation distance, and $\bar{u}_m$ is the mean wind speed of the two points.[58] The fraction in the exponential is also referred to as the reduced frequency. In the TurbSim implementation, the decay coefficient is dependent on the velocity component, but independent of the separation direction. The decay coefficients obtained from measurements are used. All available vertical separation distances, 40–80, 40–60, and 60–80 m, are used to obtain these decay coefficients in order to reduce the statistical uncertainty. A further reduction in uncertainty would be expected if even more distances or longer periods were available. However, following the mentioned approach, we achieve decay coefficients specific for the selected situations, as given in Table 3. More advanced coherence models may be considered in further work. As highlighted by Cheynet et al.,[16] the Davenport model seems to fit quite well to the uu coherence and vv coherence at FINO1.

The mean wind speeds from the measurements at 80-m height, together with a wind profile, are added to the turbulence field in TurbSim. A logarithmic wind profile (Equation 2) is chosen, due to its dependence on stability (Equation 3). The roughness length is calculated from 40 and 80 m sonic anemometer measurements. We assume that the largest accessible separation distance is more representative for the shear profile over the rotor. Its robustness is, however, also checked towards the 60 m mean wind speed. The simulations are run with the same spatial and temporal resolution as the runs with the Kaimal spectrum and exponential coherence model.

2.4 | Large-eddy simulations

LES of the atmospheric boundary layer are performed to generate another source of inflow winds for this study. LES is attractive because it solves a filtered form of the governing equations of fluid flow and it directly resolves the larger, more important, energy-containing turbulent scale of the flow. Directly resolving all turbulent scales of the atmospheric boundary layer, down to the energy-dissipating scales, is not computationally possible now or in the foreseeable future, so LES is the best alternative. The effect of the unresolved scales on the resolved scales is modeled using a subgrid-scale turbulence model.

LES is performed using the NREL's Simulator fOr Wind-Farm Applications (SOWFA),[27] which is built upon the OpenFOAM CFD toolbox.[59] OpenFOAM provides all the base functionality of SOWFA through a wide variety of C++ classes for solving complex partial differential equation systems, and SOWFA provides specialized solvers, turbulence models, boundary conditions, forcings, and turbine models for performing atmospheric and wind plant LES. The incompressible governing equations are solved, but the momentum equation includes a Boussinesq buoyancy term, requiring the solution of a potential temperature equation. The system of governing fluid flow equations are discretized using the cell-centered, collocated variable finite volume method. Time advancement uses implicit backward-in-time discretization. A predictor–corrector approach involving sequential solutions for momentum, pressure, temperature, and turbulence quantities with a pressure projection step is used. Although we always use hexahedral meshes, the code's unstructured mesh handling allows us to add regions of arbitrary mesh refinement to resolve more turbulent content.

To generate the inflow winds, we perform periodic atmospheric LES in which the atmospheric boundary layer within a volume extending from the ground to 0.75–2 km vertically and 1.5–5 km horizontally is simulated. The domain size is dictated by the atmospheric stability, which dictates the largest turbulent structures present. The ground is modeled as a rough surface that applies stress to the flow above using Monin–Obukhov scaling laws. Heat flux at the surface can also be applied to achieve different atmospheric stability. A pressure gradient force combined with a

TABLE 4 Large-eddy simulations computational domain and grid sizes

First step: Region covering the largest turbulent structures present							
Stability	Lx (m)	Ly (m)ᵤ	Lz (m)	T (s)	T (s)	dx (m)	dz (m)	dt (s)
Unstable	5000	5000	2000	15000	10	10	10	0.25 (18 m/s), 0.333 (12.5 m/s), 0.5 (7.5 m/s)
Neutral	5000	5000	1000	15000	10	10	10	0.25 (18 m/s), 0.333 (12.5 m/s), 0.5 (7.5 m/s)
Stable	2500	1500	750	20000	5	5	5	0.125 (18 m/s), 0.25 (12.5 m/s), 0.5 (7.5 m/s)
Second step: Region of localized grid resolution which captures smaller-scale flow features							
Unstable	1250	300	300	5000	1.25	1.25	1.25	0.03125 (18 m/s), 0.04 (12.5 m/s), 0.0625 (7.5m/s)
Neutral	1250	300	300	5000	1.25	1.25	1.25	0.03125 (18 m/s), 0.04 (12.5 m/s), 0.0625 (7.5m/s)
Stable	1250	300	300	5000	1.25	1.25	1.25	0.03125 (18 m/s), 0.04 (12.5 m/s), 0.0625 (7.5m/s)

simple controller is applied to drive the wind to a desired mean wind speed and direction at hub height. The initial potential temperature profile used is important, particularly because it dictates the location of the capping inversion and its strength, which then dictates atmospheric boundary layer height. The stability, mean profile shape, and turbulence characteristics cannot be precisely selected, but are the result of the chosen pressure gradient force, surface roughness, surface heat flux, and capping inversion height/strength. Depending on the stability, the simulations are run between 4 and 6 h to achieve a fully developed turbulent atmospheric boundary layer. By adjusting the simulation parameters described above over which we have control, the desired general flow characteristics (defined in Section 2.5) can be achieved. Details on how exactly we matched these conditions are discussed in Section 2.5.2.

It is the nature of LES that the solution changes as the computational mesh resolution is changed. The solution can also be affected by artificially constraining the largest turbulent scales. We chose overall domain sizes compatible with the largest scales that the different simulated conditions would produce. For example, unstable conditions produce large and tall convective structures requiring a larger and taller domain, whereas stable conditions have largest turbulent structures that are much smaller with a shallower boundary layer depth necessitating the use of a much smaller domain with higher resolution. The grid resolution necessary to well capture a turbulent atmospheric boundary layer, though, is not sufficient to capture the smaller turbulent scales that are important for predicting wind turbine loads. Because it would be computationally infeasible to use higher resolution throughout the entire computational domain, we locally refine down to higher resolution where the velocity is to be sampled, taking care that there is enough upstream fetch for the smaller scale turbulence to properly form. The simulations with the refinement box are run with somewhat finer time and space resolution as the Mann and TurbSim simulations. The computational domain and resolution details of LES are summarized in Table 4.

Within the refinement volume, yz planes are saved for further use. Taylor's hypothesis is assumed in order to achieve a wind speed volume by concatenating the extracted yz planes of velocity data in a format equivalent to the output of the DTU Mann Generator.

2.5 | Data selection and matching

2.5.1 | Measurements

We select nine time series for further use close to and above rated wind speeds for the DTU 10-MW reference turbine in stable, unstable, and neutral atmospheric conditions. In addition to wind speed and stability, the selection is based on turbulence intensity, stationarity, and quality of the data, as described in the following paragraphs. We choose situations with characteristics obtainable by LES, as we want to compare the effect on the dynamic response of a wind turbine of varying turbulent wind fields, disregarding the dominating effect of different wind profiles and turbulence intensities. Figure 3 shows the distribution of the available hourly data with respect to wind speed and turbulence intensity. In this figure, data blocks of 1-h duration are presented, with starting time every full and half hour. Thus, each 30-min period may be represented twice (10:30–11:00 both in the 1-h data blocks starting at 10:00 and 10:30). This is a meaningful presentation when used for selections, but one should be aware that the figure does not show the representative yearly statistics of FINO1. The turbulence intensity is calculated from 1 Hz 10-min periods averaged over each hour, where the standard deviation is calculated at 80 m and assumed constant with height. Hourly data are needed in the wind field simulations, as the outputs of the same length will further on be used for wind turbine analysis, where hourly simulations are favorable. Processed 30-min periods following each other, within the same 1 m/s wind speed bin, are grouped together in Figure 3. The selection of the mentioned 9 time series is based on characteristics at 119 m (hub height of DTU 10-MW reference turbine) of these complete hours.

The wind speed at 119 m is found by the log law (Equation 2), where the roughness length is calculated from the measured wind speeds at 40 and 80 m by solving Equation (2) for z_0. The mean thrust on the turbine increases with wind speed up to the rated wind speed, while the wind turbine controller reduces the thrust thereafter. Three mean wind speeds have been considered, below rated, approximately at rated, and above rated wind speed. The three cases are of interest for different reasons: below rated wind speed, the turbine is designed for maximum aerodynamic efficiency while the mean thrust has its maximum at rated wind speed. Above rated wind speed, a certain turbulence intensity corresponds to larger variations in the wind velocity than for the two previous cases. The below rated case is chosen at a typical wind speed at FINO1, close to 7.5 m/s. Instead of choosing exactly the rated wind speed, we choose to study the case just above, 12.5 m/s, in order to avoid being at the interface between two regions where the controller will jump between modes due to turbulence. Above rated, we choose the highest available wind speed from the processed FINO1 data set where all atmospheric stability conditions are present, 18 m/s.
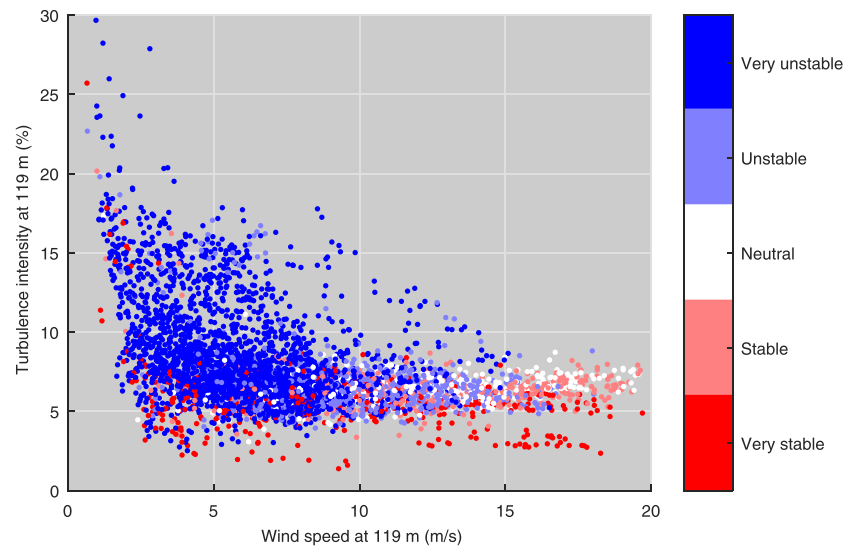
FIGURE 3 Figure used in the selection process, showing turbulence intensity as a function of wind speed for hourly periods at 119 m (TI is based on the average of six 10-min intervals of 1 Hz) [Colour figure can be viewed at wileyonlinelibrary.com]

When selecting the nine situations, confidence in stability class is also considered. Every hourly period in the processed data set is classified in terms of atmospheric stability (found from 20 Hz data) according to Table 1. However, only three stability classes are used further, where very stable and stable both are categorized as stable. The Obukhov lengths are calculated from Equation (4) by using 40 m data. We assume that MOST is valid at 40 m and that the stability at 40 m is representative for the complete rotor area. We further assume that the error of using sonic temperature as the potential virtual temperature in Equation (4) is small close to sea level. These assumptions, in addition to the dependency of the rotation method chosen, are potential sources for uncertainty in the stability classifications. In order to avoid erroneous classification, measurements well within the corresponding stability ranges are chosen for further use. We also try to find the more stable/unstable case where possible, in order to better explore the effects of stability.

Periods with typical turbulence intensity for each stability class are chosen within wind speed bins of 1 m/s, also being within the obtainable range of LES. As discussed in Section 2.1.1, we strive to match turbulence intensities at hub height in order to avoid dominating effects by the point statistics. The turbulence intensity of unstable situations is typically higher than in stable situations, as shown in Figure 3. When choosing time intervals for analysis, less weight is put on roughness length and veer. The roughness length is low above sea level, and the veer is also found to be quite low, even though it is higher in stable situations than in neutral and unstable situations.

Furthermore, an evaluation of the stationarity is included in the selection of time series. The processed 1-h periods are already expected to be quite stationary, following the processing procedure. However, the stationarity is anyway tested following a two-step process, as described in Nybø et al.[54] This test evaluates both the linear trend and the moving statistics of the time series. Finally, a manual inspection of the time series is performed, in order to ensure high-quality data for the further investigations.

2.5.2 | Large-eddy simulation

For the LES, we strive to achieve the same hub height mean wind speed, turbulence intensity, stability, and shear profile as of the nine measurement cases. As mentioned in Section 2.4, the desired mean wind speed at turbine hub height is quite easily achieved using the pressure gradient force with a simple controller. Atmospheric stability, shear, and turbulence intensity cannot be precisely controlled and depend upon the combination of pressure gradient force, surface roughness, surface heat flux, and capping inversion height/strength chosen. Therefore, we ran many cases in which we manually adjusted these parameters before we achieved conditions that matched the measurement cases well enough. In searching for parameters that resulted in a reasonable match between simulation output and observations, we began by using the surface roughness calculated from the observations, a typical capping inversion height for each stability class (a higher inversion for unstable conditions and a lower inversion for stable conditions) but with a common inversion strength for all cases, and an informed initial guess at surface heat flux based on prior experience. Generally, these initial cases produced output somewhere within the neighborhood of the target values. To fine tune the results, we ran subsequent simulations in which we primarily adjusted the surface heat flux, and sometimes, we also adjusted the surface roughness and capping inversion height, until the results were within a desired margin of agreement with observations. Admittedly, it was difficult to produce LES wind fields with high enough turbulence intensity without compromising the values of shear and stability level.

Because the LES is somewhat idealized, without the constantly varying background forcing found in nature, the low-frequency part of the turbulent spectrum often has less magnitude than that of the observations. Additionally, this may be explained by the way the mean wind speed is quite strictly controlled at hub height. The planar-averaged wind speed at hub height is driven to match desired values every time step by modulating the global background pressure gradient force. Wind speeds at different points at hub height, though, are allowed to vary freely. The low-frequency part of the spectrum is dictated by the largest turbulent structures in the atmospheric boundary layer, which under unstable conditions can be a few kilometers in length. The idea of this mean wind speed controller assumes that the averaging plane is large enough, relative to the largest turbulent structures such that enough of them are sampled onto the plane to provide a statistically converged mean wind
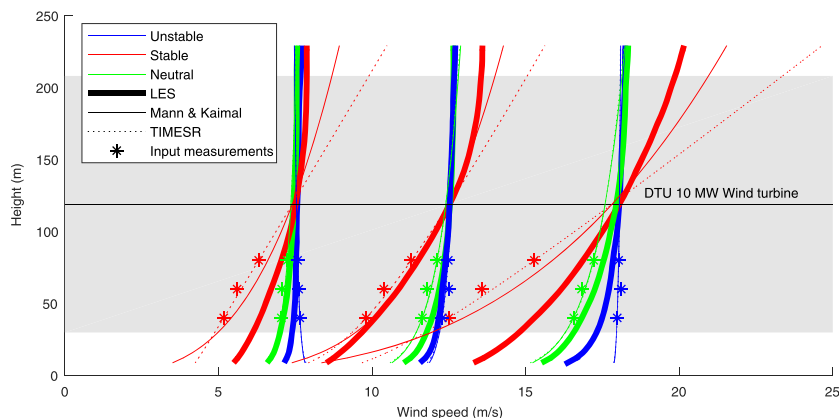
FIGURE 4 Wind profiles of all generated wind fields in all selected situations: below, close to, and above rated in various stability conditions. The color code identifies the stability regime. Thin lines: Mann and Kaimal; dashed lines: TIMESR; bold lines: LES. The stars represent the sonic anemometer measurements chosen as input. The stable and unstable versions of Mann and Kaimal should be considered as neutral flows with turbulence intensities and wind profiles adapted to the given stability. LES, large-eddy simulations [Colour figure can be viewed at wileyonlinelibrary.com]

speed. Imagine an undersampled case in which only one of these largest structures is sampled on the averaging plane. In that case, the wind speed controller would attempt to force the flow such that this structure's velocity deviation from the desired mean in the plane is driven to zero. Because spectra are derived from point measurements, a point measurement in the plane would then effectively contain less wind speed fluctuation from this large turbulent structure. To remove this effect completely, extremely large domains are required. Moreover, there is less energy in the high frequency range of the velocity spectra of the LES than in measurements because LES, by definition, does not resolve the smaller turbulent scales, both in space and time. However, this part of the energy spectrum has minimal impact on the fatigue loads of wind turbines, as mentioned in Sections 2.1.1 and 2.1.4.

2.5.3 | Standard wind fields

Also in the standard simulations, using the DTU Mann Generator and TurbSim, we strive to achieve the same hub height wind speed, shear profile, and hub height turbulence intensity as for the corresponding measurements. This is both due to their impact on results, as mentioned for LES, and because these parameters are usually somehow related to site measurements in industrial design procedures.

We choose to scale the wind profiles of the simulated wind fields with the power law, according to the IEC design standard.[1] However, the shear exponent is fitted to the measurement situations. The wind speed at hub height from TIMESR is used in the scaling procedure in order to achieve the exact same wind speed at this height. The turbulence intensity is scaled with a height independent parameter to match the turbulence intensity of the measurements at hub height. We use the turbulence intensities from the average of six 10-min, 1-Hz blocks from measurements to scale the Mann and Kaimal wind fields of 1 h and 10 Hz. As Kaimal and Mann are stationary models, there is very little difference between the turbulence intensity from the mentioned frequency ranges of these fields. The scaling is done by TurbSim for the Kaimal wind fields, whereas the same procedure is followed manually for the Mann wind fields.

3 | RESULTS AND DISCUSSION

3.1 | Overview of situations

The following figures give an overview of the chosen situations. Figure 4 shows the mean wind profiles aimed to fit the chosen below rated, close to rated, and above rated wind speeds at the hypothetical hub height of the 10-MW DTU wind turbine of 119 m. As mentioned in Section 2, the power law is used for Kaimal and Mann scaling, with the empirical exponent fit to measurements. The logarithmic law is used for the TIMESR runs, explaining the minor difference to the standard models.

Figure 4 shows clearly the expected stability dependency of the wind profiles, with an increase in vertical wind shear from unstable over neutral to stable atmospheric conditions. All methods agree well for neutral and unstable atmosphere, whereas the discrepancies increase for stable conditions. In particular, the LES profiles for stable conditions deviate distinctly from the other methods and the basic measurements. This is a natural consequence of prioritizing point statistics, wind speed, and turbulence intensity at hub height, in the matching of LES and measurements.

Figure 5 shows the wind speed distribution at the hub location, in addition to key information of the different wind fields (average wind speed, turbulence intensity, and stability expressed by the Obukhov length) for all investigated situations. As expected, high standard deviations are observed for the unstable situations, whereas the stable situations have larger kurtosis. This is related to the larger eddies expected in unstable conditions relative to stable. The wind speed and standard deviation of the Kaimal and Mann fields are scaled in order to match the TIMESR simulations, but we still observe some minor deviations in the turbulence intensity. The standard wind fields assume a neutral atmosphere; thus, the Obukhov lengths are not given. We observe that the probability density functions are very similar for the two standard models. In comparison with TIMESR, there is higher kurtosis and minimal skewness.

For the LES, we observe that the turbulence intensity is far from TIMESR in several situations, even though we aimed at matching hub statistics. In particular, the neutral situations from the measurements are very turbulent, being close to the unstable situations at close to and
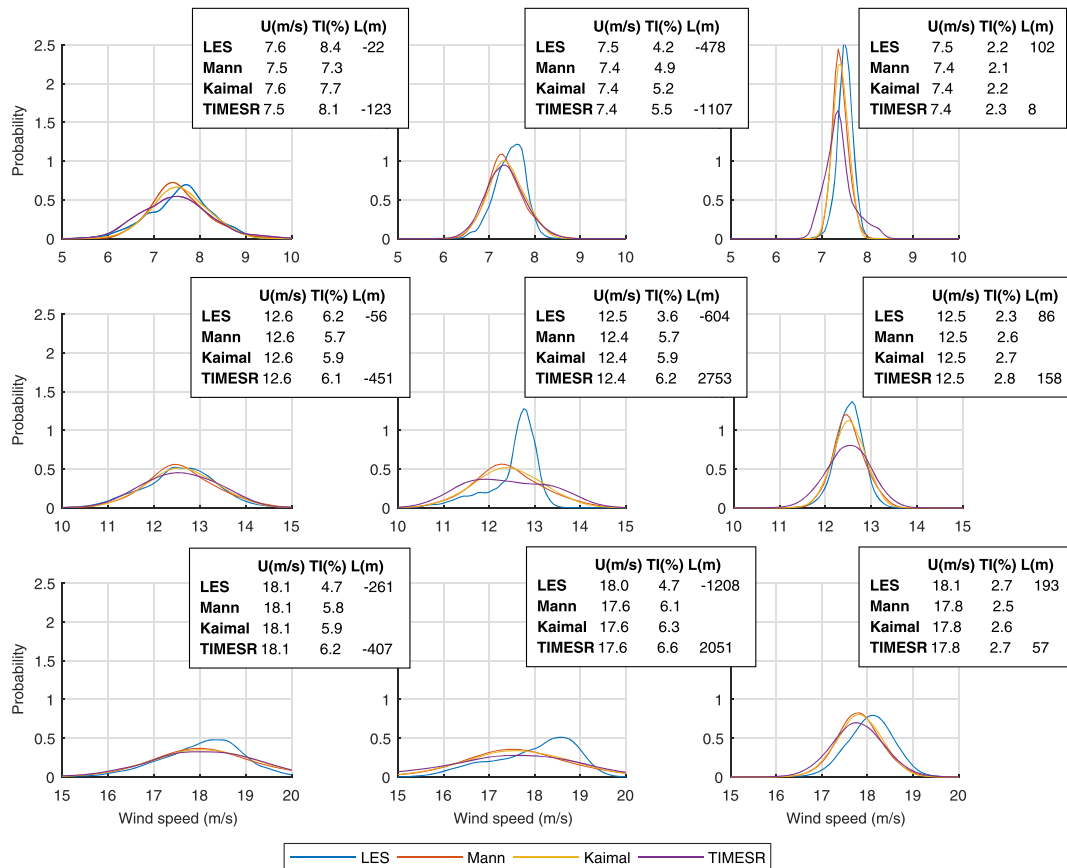
FIGURE 5 Wind speed distribution of all generated wind fields at the hub location for unstable (left panels), neutral (center panels), and stable conditions (right panels). TI is calculated based on 10 Hz data over the average of six 10-min averaging intervals. The stable and unstable versions of Mann and Kaimal should be considered as neutral flows with turbulence intensities and wind profiles adapted to the given stability. LES, large-eddy simulations [Colour figure can be viewed at wileyonlinelibrary.com]

above rated wind speed. This is unfortunate because it hinders further comparisons between conditions of different atmospheric stability. The reason for the high measured TI in neutral conditions is not fully understood. These turbulent offshore conditions are difficult to achieve with LES. As mentioned in Section 2.5.2, the turbulence intensity is an output of LES and cannot be directly controlled by the inputs. The turbulence intensity is tuned towards the desired value by modifications in the surface roughness and the surface heat flux. However, compromises had to be made in order to achieve close to desired stability and shear profiles.

In contrast to the measurements, the Obukhov lengths of the LES are not strictly within the ranges of Table 1. In the neutral cases below and close to rated, the surface flux had to be increased significantly in order to achieve higher turbulence intensity. This leads to a decrease of the absolute Obukhov length to less than 1000, which is the neutral limit in Table 1. However, the absolute value of the Obukhov length from the LES in these cases is far higher than for the unstable cases. There are therefore distinct differences in the wind fields of the unstable, neutral, and stable cases. Moreover, they are within the neutral and near-neutral range of the classification ranges of Gryning et al.[40]

From the wind distributions in Figure 5, we also observe major differences between LES and TIMESR. In most situations, the LES distributions have distinct negative skewness and remarkably higher kurtosis. As for the comparison with the standard models, this reflects even lower standard deviations. Larger differences are found in the situations where the standard deviation deviates more, for example, at 12.5 m/s, in a neutral atmosphere. The LES are very stationary, most likely due to the method of controlling the wind speed in the precursor runs, mentioned in Section 2.4. A less strict control mechanism would probably lead to wider tales of the LES distributions.

3.2 | Comparison of wind fields

3.2.1 | Turbulent structures

Figure 6 shows xy planes close to hub height of the different wind fields for the close to rated wind speed of 12.5 m/s. The full lateral section of the wind fields is shown, whereas the longitudinal direction is represented by a snapshot of around 440-m length (corresponding to a time period of ~35 s), taken from the center of the wind field. The statistical characteristics of the wind fields are better explained by Figure 5, whereas Figure 6 gives a qualitative perspective of the structures of different simulators and atmospheric stability conditions.

We observe that the TurbSim wind fields (Kaimal and TIMESR) contain more fine turbulent structures than the Mann wind fields. The wind fields generated by LES show even coarser turbulent structures, which can, at least partly, be explained by the coarser spatial and temporal
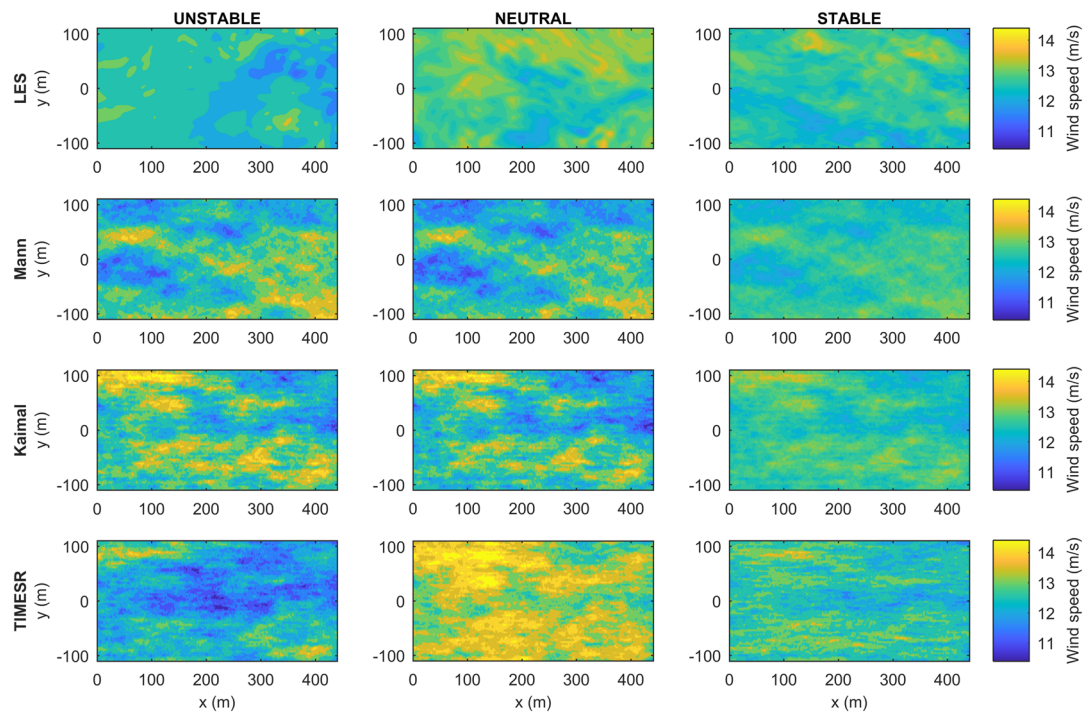
FIGURE 6 xy planes close to hub height of the 12.5 m/s wind fields in various stability conditions at full lateral domain size (220.5 m) and for a snapshot in the longitudinal direction of 441-m length (corresponding to about 35 s). The x and y axes are scaled identically. The stable and unstable versions of Mann and Kaimal should be considered as neutral flows with turbulence intensities and wind profiles adapted to the given stability. LES, large-eddy simulations [Colour figure can be viewed at wileyonlinelibrary.com]

resolution of the domain. We see also a stretching of the eddies in the longitudinal direction in most of the wind fields, which is realistic considering the presence of a vertical shear profile.

When comparing across atmospheric stability conditions, we observe minor differences between the different runs of Kaimal and Mann. The seeds are equal in the different runs, and as stability is not accounted for by the simple models, only the turbulence intensity and mean wind speed can cause these minor differences. For instance, we see less variation of the wind speed in the stable situation with lower turbulence intensity (neutral and unstable turbulence intensities are almost equal in TurbSim and Mann runs at close to rated wind speed).

The same differences can be recognized in the TIMESR wind fields. The phase angles of the simulated points are determined by the seed, before they are correlated to the phase angles of the 80 m input time series by the Davenport coherence model. When the same seed is used, similar wind fields are therefore expected, with some deviations due to the variation of the phase angles and decay parameters of the inputs. Except for the difference in wind speed variation, explained by the difference in turbulence intensity, we may observe that the more stable the atmosphere, the finer and longer turbulent structures are observed in the TIMESR wind fields. This is according to expectations for the different atmospheric stability conditions.

In agreement with Doubrawa et al.,[9] we observe larger structures in the unstable LES case. As for the TIMESR cases, we also observe stretched structures in the longitudinal direction for the more stable the atmospheric conditions. Although excluded from this article, the same qualitative results are found in the structure plots of wind speeds below and above rated.

3.2.2 | Spectral analysis

In agreement with the turbulence intensities given by Figure 5 (middle), Figure 7 shows that the variance of the Kaimal, Mann, and TIMESR wind fields is similar. It is clearly visible that LES is not able to represent a realistic power level at frequencies above 0.1–1 Hz, consistent with Doubrawa et al.[9] and Sim et al.[29] This is due to the size of the refinement volume, as explained in Section 2.1.4. At periods larger than a few seconds, more important for floater behavior, the energy level is closer to the TIMESR wind fields in all situations. In the neutral 12.5 m/s case shown in Figure 7, the LES spectrum is slightly shifted towards lower energy levels in correspondence with the lower turbulence intensity achieved in the simulations. Spectral analysis of other wind speeds and atmospheric stability conditions (not shown) confirms that the energy level at low frequencies is highly dependent on the turbulence intensity. As expected, the energy level in stable situations is lower than in unstable situations.

Figure 8 (left) shows the co-coherence of an example TIMESR wind field compared with the input measurements at the largest available height as function of reduced frequency ($\frac{f\delta}{\bar{u}_m}$). This figure illustrates the difference between the highly fluctuating co-coherence values from the input measurements and the smooth exponential decay from the derived TIMESR data set. This should be kept in mind when interpreting the corresponding curves that are compared with the coherence of the standard and LES data sets in Figures 9 and 10. As mentioned in Section 2.3.4, the fit to the Davenport model includes statistical errors that decrease with the length of the time series and number of time series. The
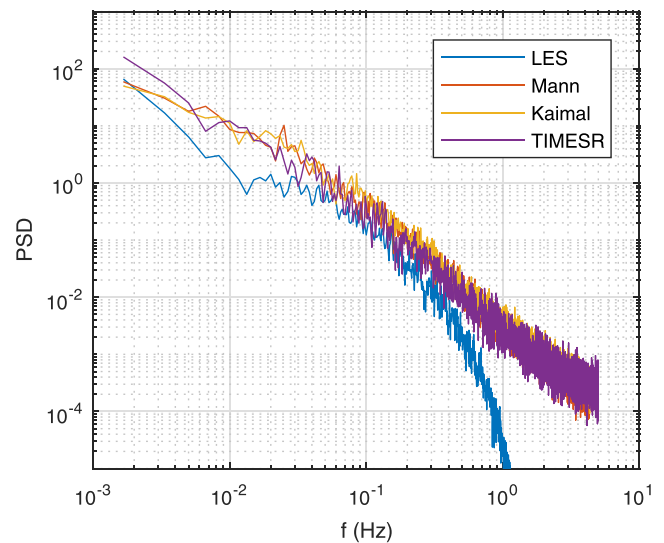
FIGURE 7 Energy spectrum at hub location of the neutral 12.5 m/s case. LES, large-eddy simulations [Colour figure can be viewed at wileyonlinelibrary.com]
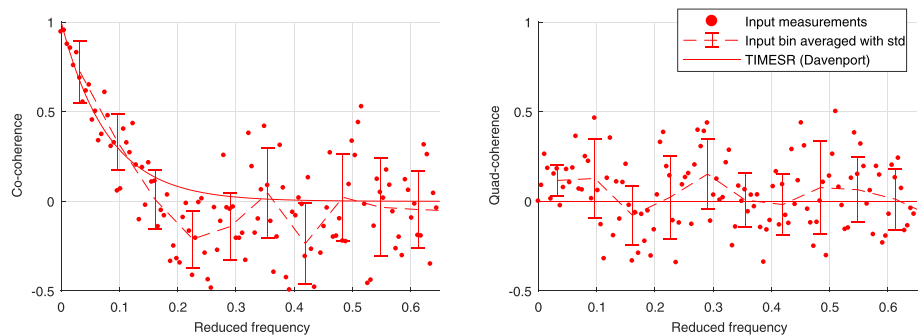

FIGURE 8 Vertical coherence of measurements between 80 and 40 m for the neutral 12.5 m/s case [Colour figure can be viewed at wileyonlinelibrary.com]

Davenport coherence model forces the co-coherence to unity at zero reduced frequency, which fits well with the measurements in Figure 8 (left), but is often a poor assumption especially for large crosswind separations.[60] Figure 8 (right) shows the quad coherence of the same situation, often excluded due to its insignificance compared with the co-coherence. Both the Davenport model and the Kaimal model ignore the quad coherence, whereas the Mann model formulates the quad coherence, but only in the vertical direction. The vertical shear in the formulation of the Mann model causes a phase shift for time series separated vertically, but not laterally. According to the results of Figure 8 for 40-m separation distance, also observed for other wind speeds and atmospheric conditions, the quad coherence is significantly smaller than the co-coherence. However, the phase shift is not negligible. For larger separations, it may be even more significant. This may have importance to the loads on a wind turbine blade, as the turbulent velocity fluctuations at a certain frequency will not have the same phase along the length of the blade. Further, it is observed from Figure 8 (left) that the co-coherence may be negative in certain reduced frequency ranges. This implies an opposite phase of the turbulent velocity components. This effect will change the dynamic load pattern along a wind turbine blade significantly.

Assuming that the fitted Davenport coherence represents the coherence of the measurement situations fairly, we may evaluate and compare the standard and LES wind fields with the TIMESR fields on the basis of Figures 9, 10, and 11. It should first be mentioned that the coherence reduces drastically with reduced frequency in all models, being insignificant at reduced frequencies higher than 0.5 in all situations. As mentioned earlier, the lowest eigenfrequencies of bottom fixed turbines are about 10 revolutions per minute, corresponding to reduced frequencies above the limit of insignificance just mentioned. The impact of coherent structures is therefore expected to have larger effect on floaters, having far lower eigenfrequencies. The longest natural period relevant for floaters is related to the rigid body modes of motion and is typically about 100 s. This corresponds to reduced frequencies in the range 0.05 for 18 m/s at 0.5 D separation to 0.24 for 7.5 m/s at 1 D.

As shown by Figures 9 and 10, the co-coherence of the TIMESR wind fields is, as expected, higher for the unstable situations, whereas the co-coherence of the stable situations falls steeply with the reduced frequency. The eddies of an unstable atmosphere are by far larger than in a stable atmosphere, explaining this larger co-coherence over distances comparable with the rotor diameter. This trend is consistent with the findings of Cheynet et al.[16] As shown by Figure 5, the neutral and unstable TIMESR cases have similar characteristics at close to and above rated wind speeds, which is also the case for the co-coherence. The Davenport model is independent of the separation distance, except through the reduced frequency, illustrated by the equal curves in the horizontal pairs of subfigures in Figures 9 and 10. It is also independent of direction; thus, the TIMESR curves are equal in Figures 9 and 10.

Both the Mann model and the Kaimal model are independent of stability, shown by a single curve for each model in Figures 9 and 10. In contrast to the Davenport model, they are both dependent on the separation distance, resulting in less co-coherence with larger distance. Mann shows significant co-coherence at low reduced frequencies, but falls off steeply, whereas Kaimal starts off with lower co-coherence, but decays
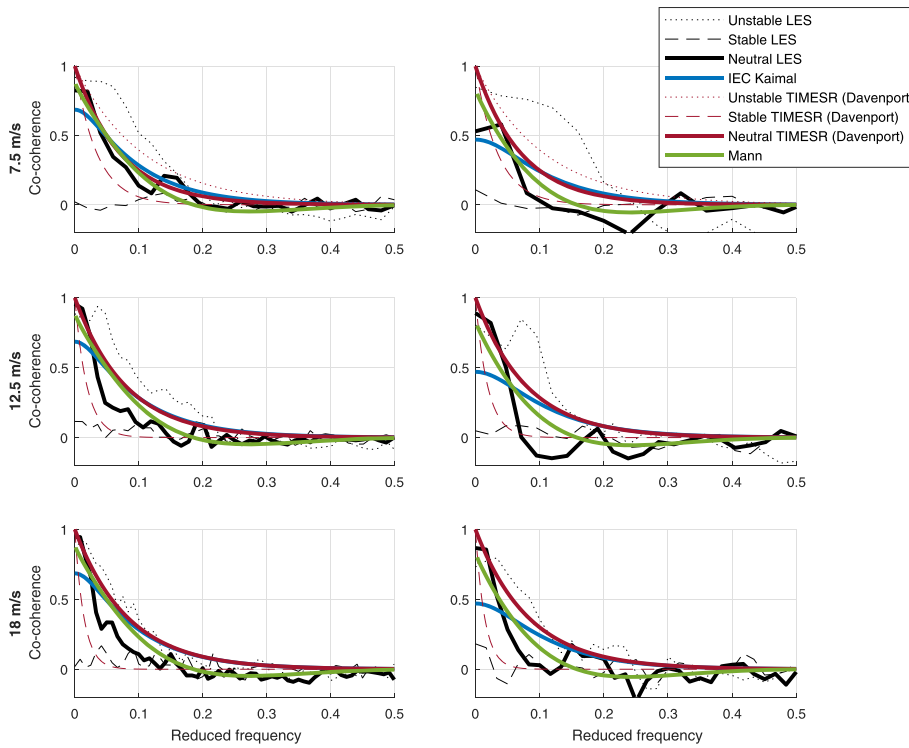
FIGURE 9 Vertical co-coherence at 0.5 (left) and 1 diameter (right) separation distance for all generated wind fields. IEC, International Electrotechnical Commission; LES, large-eddy simulations [Colour figure can be viewed at wileyonlinelibrary.com]
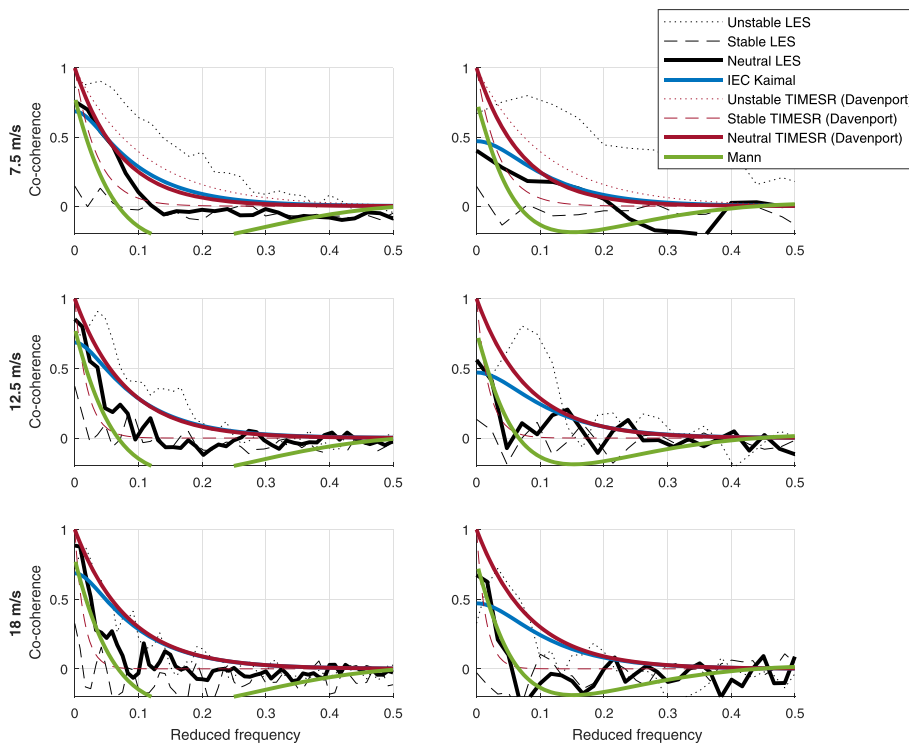

FIGURE 10 Lateral co-coherence at 0.5 (left) and 1 diameter (right) separation distance for all generated wind fields. IEC, International Electrotechnical Commission; LES, large-eddy simulations [Colour figure can be viewed at wileyonlinelibrary.com]

slower. As the Davenport model always starts off at unity, the Mann model matches the TIMESR runs consistently better at the lowest reduced frequencies. However, this frequency range is not the most important for dynamic response, being lower than the natural frequencies of both bottom-fixed and floating wind turbines. Whether the Mann or Kaimal co-coherence fits better with TIMESR at higher frequencies depends on the stability of the TIMESR runs. The Kaimal co-coherence is closer to the neutral and unstable TIMESR runs from the intersection between Mann and Kaimal in both separation directions. This intersection appears at a reduced frequency close to 0.05 in the vertical co-coherence plots (Figure 9) and even closer to zero in the lateral plots (Figure 10). Mann matches the stable TIMESR curves overall better for the vertical co-coherence. Considering the co-coherence of lateral separations, Mann falls sharply, matching the stable case even better at low frequencies, but tends to fall below zero, which is not the case for Davenport. Kaimal as TIMESR, however, is independent of separation direction. From both figures, we observe a close to perfect match between Kaimal and neutral TIMESR at reduced frequencies higher than 0.05–0.15.

FIGURE 11 Vertical (left) and lateral (right) quad-coherence at 1 diameter separation distance for 12.5 m/s. LES, large-eddy simulations [Colour figure can be viewed at wileyonlinelibrary.com]
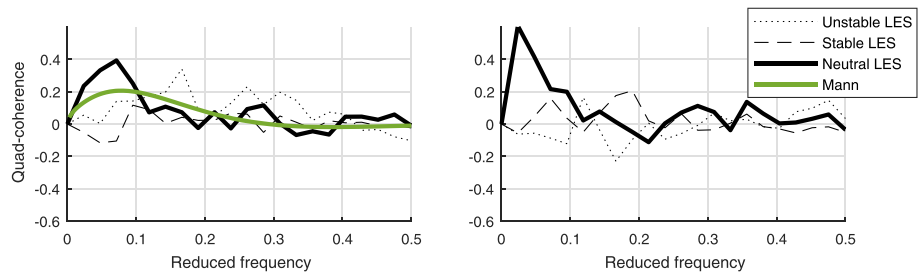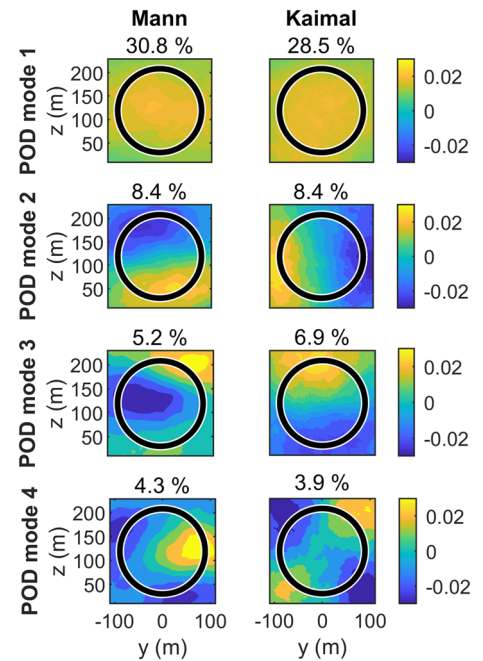

FIGURE 12 POD modes 1–4 of Kaimal and Mann wind fields for the 12.5 neutral case. Explained variation per mode is given above each subplot. POD, proper orthogonal decomposition [Colour figure can be viewed at wileyonlinelibrary.com]

The evaluation of Kaimal and Mann so far is based on comparison with the measurements fit to a simple exponential model with all the expected statistical errors, but it may be as relevant to compare them with more advanced simulations such as LES. The coherence of the LES is averaged over all available vertical and lateral separations in order to reduce noise. The points furthest up and most right in the wind fields are used as reference in the cross-spectrum calculations. The co-coherence of the different LES fields follows the same pattern as TIMESR, with significantly stronger co-coherence for the unstable atmospheric conditions. This is consistent with the findings of Doubrawa et al.,[9] also comparing the coherence of LES wind fields of various stability conditions. In contrast to the TIMESR runs based on the Davenport model, the co-coherence is different to unity at zero reduced frequency. Consistently with the general trend, the co-coherence at very low frequencies is also lower the more stable the atmosphere. We even observe close to zero co-coherence in the most stable cases in both separation directions, for all reduced frequencies. In accordance with Figure 5, there is a larger difference between the unstable and neutral characteristics of the LES. For the largest separation distances (Figures 9 and 10 right), the co-coherence starts off at a lower co-coherence at zero reduced frequency, in consistency with Mann and Kaimal, but stays at a higher level for a larger range of frequencies. This is especially evident in the unstable case below rated. For neutral and unstable conditions, in the LES runs, it is found that the higher the wind speeds, the faster the decay of co-coherence, both vertically and laterally. This trend is similar for the stable case of TIMESR, but is less evident at other atmospheric conditions. As expected for the simple standard models, they fit better to the neutral LES cases. In most frequency ranges of the vertical co-coherence plots, Mann is a better fit to the neutral case of LES, in contrast to the comparisons with TIMESR where Kaimal was a better fit. For the lateral separations, such a general clear conclusion does not exist, as the neutral LES typically lays between the Kaimal and Mann co-coherence plots. Compared with the unstable and stable LES cases, Mann and Kaimal are both far off, with the closest match being the one resulting in higher or lower co-coherence, respectively.

The quad coherence is, as mentioned, only present in the Mann and LES wind fields. Figure 11 shows the vertical and lateral (only LES) quad coherence at 1 diameter separation distance for 12.5 m/s. Equivalent results are found for 7.5 and 18 m/s. As expected, the co-coherence (Figure 9 [right middle] and Figure 10 [right middle]) is significantly higher than the quad coherence in most wind fields. Still, the phase shift of Mann and some of the LES fields is not negligible for low frequencies where the coherence is most significant. We observe that the quad coherence of Mann is positive when the highest point is used as reference. This is consistent with the measured vertical coherence shown in Figure 8. It is more challenging to analyze the LES fields with all the present noise, but the quad coherence appears to be likewise positive. However, as for the co-coherence, the stable quad coherence is negligible, whereas the unstable and especially neutral quad coherence is more significant. To summarize, we observe a non-negligible quad coherence both from measurements and LES, which causes a phase shift that is
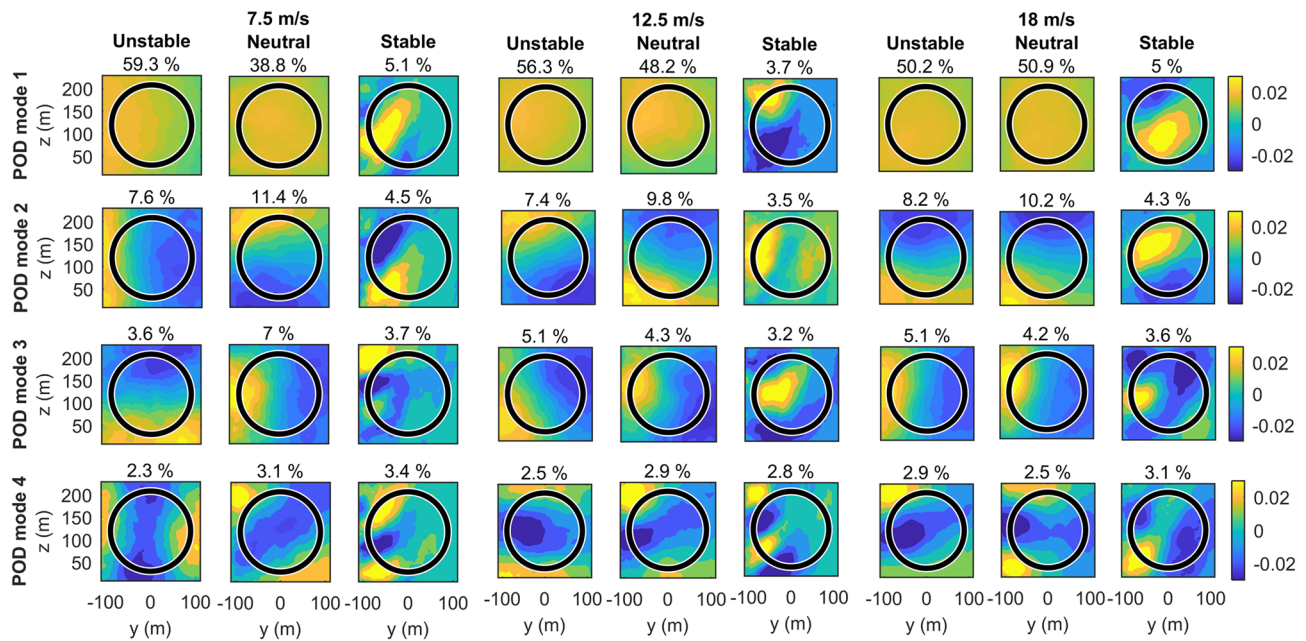
FIGURE 13 POD modes 1–4 of large-eddy simulation wind fields for the 12.5 m/s case in all atmospheric conditions. Explained variation per mode is given above each subplot. POD, proper orthogonal decomposition [Colour figure can be viewed at wileyonlinelibrary.com]

expected to have an impact on the dynamic response of offshore wind turbines. The Kaimal and TIMESR wind fields used in this study are not able to reflect this. Response analysis must be performed in order to assess the impact of the phase shifts and to compare the impact of the different quad coherence formulations.

3.2.3 | Proper orthogonal decomposition

As mentioned in Section 2.1.5, POD modes may illustrate coherent structures in turbulent flows. In Figures 12, 13, and 14, the first four POD modes and the amount of variation explained by each of these modes are shown for the various wind fields. Being independent of stability, and using the same seed for all wind speeds, the POD modes and the amount of variation explained by each mode of Kaimal and Mann are approximately equal for all wind fields. The neutral 12.5 m/s case is illustrated in Figure 12. Almost one third of the variation of the wind fields of both models is explained by the first mode. The Mann modes seem to be stretched in the lateral direction, whereas Kaimal is more centered around the hub. Furthermore, Kaimal has the extremes outside the rotor diameter (illustrated by the black circles), whereas the extremes of the Mann modes tend to appear inside the rotor area. We expect that this may cause higher loads on the wind turbine. Our findings are consistent with those of Bachynski and Eliassen[7] and Eliassen and Andersen.[14]

Studying the POD modes of all simulators, we observe several similarities, especially when disregarding the stable case of LES. The number of coherent structures increases with the number of modes, while the size of these structures decreases. The first modes explain a major part of the variation in the wind fields. Among the general differences, we observe that the TurbSim wind fields are more fine structured than Mann, which again is more fine structured than LES, coinciding with the observations in Figure 6. Moreover, we observe that TIMESR and LES, similar to Kaimal, but in contrast to Mann, typically have extremes outside the rotor diameter. This is dependent on the domain size chosen relative to the rotor diameter. In the first mode, we observe no clear stretching of the pole in neither LES or TIMESR. For the second and higher modes, there are typically dipole structures that appear in opposite direction relative to each other in the second and third modes. These are both observations coinciding with Kaimal, but different to Mann. The shape of the POD modes and the magnitude of explained variation, based on Kaimal, are generally in better agreement with LES and TIMESR than for Mann. We may therefore conclude that Kaimal represents the modes most realistically, but still with large differences depending on stability, especially regarding the part explained by each mode.

When comparing the atmospheric stability conditions, we observe that the mode shapes in the neutral and unstable cases are similar both in LES and TIMESR. Larger parts of the variation are explained by the first modes in most of these situations, meaning that these modes contain more turbulent kinetic energy relative to the stable situations. This is expected based on the similarities seen in previous figures as well. However, we see distinct differences to the stable cases, especially for the LES. The dominance of a few energetic modes are far less pronounced in these cases. This is consistent with the results shown in Figures 9 and 10, where the co-coherence is negligible for the stable LES cases.
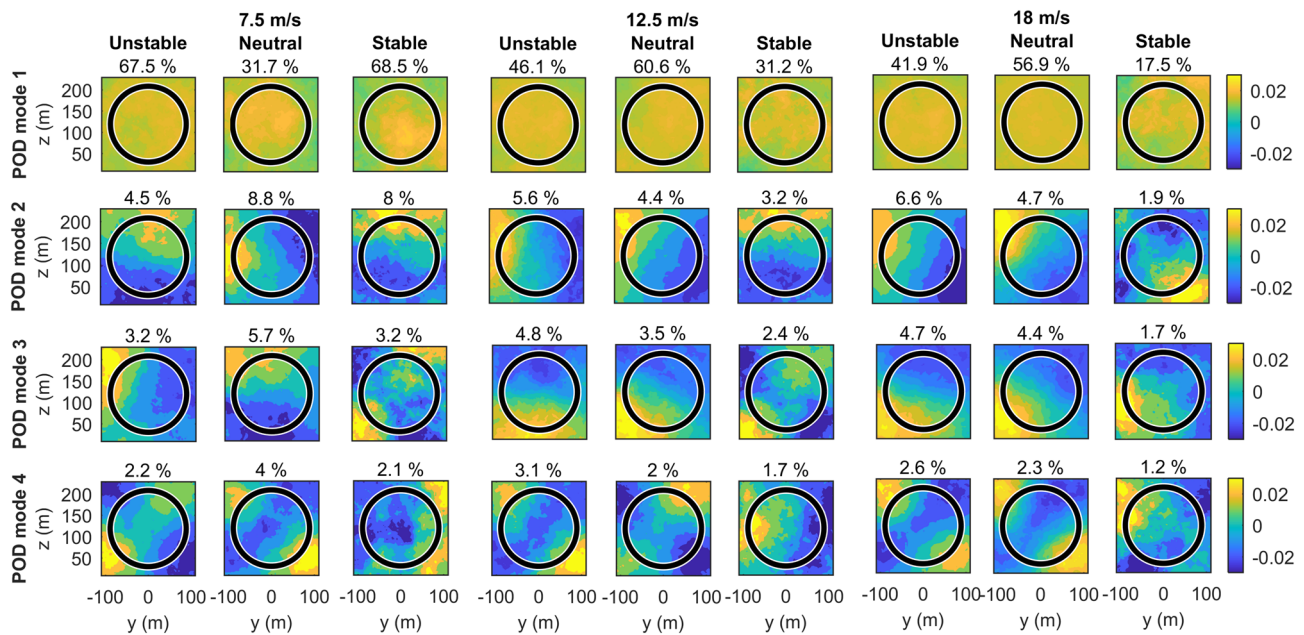
FIGURE 14 POD modes 1–4 of TIMESR wind fields for the 12.5 m/s case in all atmospheric conditions. Explained variation per mode is given above each subplot. POD, proper orthogonal decomposition [Colour figure can be viewed at wileyonlinelibrary.com]

4 | CONCLUSIONS

The development towards larger, more flexible, and floating wind turbines offshore triggers the need for an efficient and appropriate way to model the inflow conditions with realistic turbulent structures over the full stability range in an offshore environment. In this study, we have evaluated different wind field simulation techniques commonly used by the industry from both a meteorological and an offshore wind turbine response perspective. The wind fields recommended by the IEC wind turbine design standard, the Mann spectral tensor model and the Kaimal spectral and exponential coherence model, are compared with measurements and LES. Point measurements from the offshore mast FINO1 are used as input to the wind field generator TurbSim by using the TIMESR method. The four generation methods (Mann, Kaimal, TIMESR and LES) are used to create wind fields of three mean wind speeds in order to evaluate the differences in the main load regimes for a large offshore wind turbine: below, close to, and above rated wind speed. The standard wind fields, assuming neutral stratification, are compared with TIMESR and LES wind fields at various atmospheric stability conditions.

Our findings show expected differences between the various stability conditions in the LES and TIMESR wind fields. The unstable wind fields have less wind shear, higher turbulence intensity, and larger structures than the neutral and stable ones. More significant coherent structures are also found in the unstable situations. This is obvious from the temporal and spatial distributions of coherence, illustrated by high values of the frequency-dependent co-coherence and significant dominance of the first POD modes.

Significant coherent structures in the along-wind direction are obtained by all models. As expected, the standard wind fields represent the neutral situations better than the unstable and stable ones. Considering the co-coherence as function of reduced frequency, we cannot conclude whether the Kaimal or Mann model is most realistic. This is due to conflicting results when comparing the standard models with TIMESR and LES, respectively. Moreover, the LES co-coherence is noisy and the measurements may not be well represented by the fitted Davenport model. It is furthermore worth noticing that a nonzero quad coherence is only obtained by LES and Mann (vertically) models. The phase shift of the coherence may have significant impact on the loads of a wind turbine, which TIMESR and Kaimal are not able to represent. Considering the POD modes, we also see great similarities between Mann and Kaimal. However, by studying the structures of the first POD modes, Kaimal appears to be a better match to TIMESR and LES than Mann.

Neither the TIMESR nor LES wind fields can be considered as completely realistic representations of offshore wind fields. There is a need for measurements that better characterize coherence, both vertically and horizontally and over a distance on the order of modern large offshore turbines, in order to better compare models with measurements. A corresponding field campaign, with central participation of several authors of this manuscript, is at the moment ongoing. Three scanning lidar systems are deployed in a triangular setup at the Norwegian west coast, operating in a synchronized mode to measure lateral and vertical coherence in the wind field up to 3 km offshore. LES is emerging as a valuable tool as graphics processing unit (GPU) computers are becoming more readily available, but improvements are necessary in order to be able to easily tune inputs to produce desired outputs of shear and TI observed offshore. Anyway, a comparison of the standard turbulence models to TIMESR and LES, which are still considered more realistic, shows that it is time for more advanced turbulence models with inputs adapted to various stability conditions.

The wind field comparisons give valuable insight in the various generation methods and resulting coherent structures. It is clear that the spatial and temporal distributions of coherence differ significantly across generation methods and atmospheric stability conditions. This will have an impact on the dynamic response of large offshore wind turbines. From the results of this work, the effect of the various wind field characteristics on the response is still unclear. Further work will investigate these effects on a large bottom fixed and floating offshore wind turbine.

ORCID

Astrid Nybø https://orcid.org/0000-0002-7438-7936
Finn Gunnar Nielsen https://orcid.org/0000-0002-1576-2409
Joachim Reuder https://orcid.org/0000-0002-0802-4838
Matthew J. Churchfield https://orcid.org/0000-0001-9906-7288

REFERENCES

1. International Electrotechnical Commision. IEC 61400-1 Wind energy generation systems - Part 1: Design requirements. https://webstore.iec.ch/publication/26423. Accessed May 28, 2019; 2019.
2. International Electrotechnical Commision. IEC 61400-3-2 Wind energy generation systems - Part 3-1: Design requirements for fixed offshore wind turbines. https://webstore.iec.ch/publication/29360. Accessed May 28, 2019; 2019.
3. International Electrotechnical Commision. IEC 61400-3-2 Wind energy generation systems - Part 3-2: Design requirements for floating offshore wind turbines. https://webstore.iec.ch/publication/29244. Accessed May 28, 2019; 2019.
4. Fraunhofer. Turbine size. http://windmonitor.iee.fraunhofer.de/windmonitor_en/4_Offshore/2_technik/3_Anlagengroesse/, Accessed May 27, 2019; 2019.
5. Mann J. The spatial structure of neutral atmospheric surface-layer turbulence. *J Fluid Mech.* 1994;273:141-168. https://doi.org/10.1017/S0022112094001886
6. Kaimal J, Wyngaard J, Izumi Y, Coté O. Spectral characteristics of surface-layer turbulence. *Quart J Royal Meteorol Soc.* 1972;98(417):563-589. https://doi.org/10.1002/qj.49709841707
7. Bachynski E, Eliassen L. The effects of coherent structures on the global response of floating offshore wind turbines. *Wind Energy*. 2019;22(2):219-238. https://doi.org/10.1002/we.2280
8. Eliassen L, Bachynski EE. The effect of turbulence model on the response of a large floating wind turbine. In: ASME 2017 36th International Conference on Ocean, Offshore and Arctic Engineering; 2017; Trondheim, Norway:1–10.
9. Doubrawa P, Churchfield MJ, Godvik M, Sirnivas S. Load response of a floating wind turbine to turbulent atmospheric flow. *Appl Energy*. 2019;242:1588-1599. https://doi.org/10.1016/j.apenergy.2019.01.165
10. Godvik M. Influence of wind coherence on the response of a floating wind turbine. In: Science Meets Industry; 2016; Stavanger, Norway:1–12. http://www.norcowe.no/doc//konferanser/2016/SMI Stavanger presentasjoner/Godvik Statoil Influence of the wind coherence on the response of a floating wind turbine.pdf
11. Robertson A, Sethuraman L, Jonkman J, Quick J. Assessment of wind parameter sensitivity on extreme and fatigue wind turbine loads. In: 2018 Wind Energy Symposium; 2018; Kissimmee, Florida:1728.
12. Ropelewski CF, Tennekes H, Panofsky HA. Horizontal coherence of wind fluctuations. *Bound Layer Meteorol.* 1973;5(3):353-363. https://doi.org/10.1007/BF00155243
13. Eliassen L, Obhrai C. Coherence of turbulent wind under neutral wind conditions at FINO1. *Energy Proced.* 2016;94:388-398. https://doi.org/10.1016/j.egypro.2016.09.199
14. Eliassen L, Andersen S. Investigating coherent structures in the standard turbulence models using proper orthogonal decomposition. *J Phys Conf Ser.* 2016;753(3):32040. https://doi.org/10.1088/1742-6596/753/3/032040
15. Cheynet E. Influence of the measurement height on the vertical coherence of natural wind. In: Proceedings of the XV Conference of the Italian Association for Wind Engineering Ricciardelli F, Avossa AM, eds. Springer International Publishing; 2019; Cham:207-221.

16. Cheynet E, Jakobsen JB, Reuder J. Velocity spectra and coherence estimates in the marine atmospheric boundary layer. *Bound Layer Meteorol*. 2018;169(3):429-460. https://doi.org/10.1007/s10546-018-0382-2

17. FuE-Zentrum FH Kiel GmbH. FINO1: Forschungsplattformen in Nord- und Ostsee Nr. 1. https://www.fino1.de/. Accessed January 09, 2019; 2019.

18. Kelley N, Jonkman B. TurbSim - NWTC Information Portal. https://nwtc.nrel.gov/TurbSim. Accessed May 27, 2019; 2016.

19. Simley E, Pao LY. A longitudinal spatial coherence model for wind evolution based on large-eddy simulation. In: Proceedings of the American Control Conference; 2015; Chicago, IL, USA:3708-3714.

20. Worsnop RP, Bryan GH, Lundquist JK, Zhang JA. Using large-eddy simulations to define spectral and coherence characteristics of the hurricane boundary layer for wind-energy applications. *Bound Layer Meteorol*. 2017;165(1):55-86. https://doi.org/10.1007/s10546-017-0266-x

21. Berg J, Natarajan A, Mann J, Patton EG. Gaussian vs non-Gaussian turbulence: impact on wind turbine loads. *Wind Energy*. 2016;19(11):1975-1989. https://doi.org/10.1002/we.1963

22. Sathe A, Bierbooms W. Influence of different wind profiles due to varying atmospheric stability on the fatigue life of wind turbines. *J Phys Conf Ser*. 2007;75(1):012056. https://doi.org/10.1088/1742-6596/75/1/012056

23. Eliassen L, Jakobsen JB, Obhrai C. The effect of atmospheric stability on the fatigue life of offshore wind turbines. In: Proceedings of the Twenty-second (2012) International Offshore and Polar Engineering Conference; 2012; Rhodes, Greece:330-336.

24. Holtslag MC, Bierbooms WAAM, Van Bussel GJW. Wind turbine fatigue loads as a function of atmospheric conditions offshore. *Wind Energy*. 2016;19(10):1917-1932. https://doi.org/10.1002/we.1959

25. Holtslag MC, Bierbooms WAAM, Van Bussel GJW. Estimating atmospheric stability from observations and correcting wind shear models accordingly. *J Phys Conf Ser*. 2014;555:012052. https://doi.org/10.1088/1742-6596/555/1/012052

26. Sathe A, Mann J, Barlas T, Bierbooms WAAM, Van Bussel GJW. Influence of atmospheric stability on wind turbine loads. *Wind Energy*. 2013;16(7):1013-1032. https://doi.org/10.1002/we.1528

27. Churchfield M, Lee S. SOWFA | NWTC Information Portal. https://nwtc.nrel.gov/SOWFA. Accessed February 04, 2019; 2015.

28. Bak C, Zahle F, Bitsche R, et al. The dtu 10-mw reference wind turbine. http://orbit.dtu.dk/ws/files/55645274/The_DTU_10MW_Reference_Turbine_Christian_Bak.pdf. Accessed May 27, 2019; 2013.

29. Sim C, Manuel L, Basu S. A comparison of wind turbine load statistics for inflow turbulence fields based on conventional spectral methods and large eddy simulation. In: 48th AIAA Aerospace Sciences Meeting Including the New Horizons Forum and Aerospace Exposition; 2013; Orlando, Florida:829.

30. Irwin JS. A theoretical variation of the wind profile power-law exponent as a function of surface roughness and stability. *Atmospher Environ (1967)*. 1979;13(1):191-194. https://doi.org/10.1016/0004-6981(79)90260-9

31. Emeis S. Current issues in wind energy meteorology. *Meteorol Appl*. 2014;21(4):803-819. https://doi.org/10.1002/met.1472

32. Businger JA, Wyngaard JC, Izumi Y, Bradley EF. Flux-profile relationships in the atmospheric surface layer. *J Atmos Sci*. 1971;28(2):181-189. https://doi.org/10.1175/1520-0469(1971)028<0181:FPRITA>2.0.CO;2

33. Högström U. Non-dimensional wind and temperature profiles in the atmospheric surface layer: a re-evaluation. *Bound Layer Meteorol*. 1988;42(1):55-78. https://doi.org/10.1007/BF00119875

34. Dyer AJ. A review of flux-profile relationships. *Bound Layer Meteorol*. 1974;7(3):363-372. https://doi.org/10.1007/BF00240838

35. Monin AS, Obukhov AM. Basic laws of turbulent mixing in the surface layer of the atmosphere. *Contrib Geophys Inst Acad Sci USSR*. 1954;24(151):163-187.

36. Foken T. 50 years of the Monin–Obukhov similarity theory. *Boundary-Layer Meteorology*. 2006;119(3):431-447. https://doi.org/10.1007/s10546-006-9048-6

37. Haugen DA, Kaimal JC, Bradley EF. An experimental study of Reynolds stress and heat flux in the atmospheric surface layer. *Quart J Royal Meteorol Soc*. 1971;97(412):168-180. https://doi.org/10.1002/qj.49709741204

38. Hess GD, Hicks BB, Yamada T. The Impact of the Wangara experiment. *Bound Layer Meteorol*. 1981;20(2):135-174. https://doi.org/10.1007/BF00119899

39. Stull RB. *An Introduction to Boundary Layer Meteorology*. Dordrecht: Springer Netherlands; 1988.

40. Gryning SE, Batchvarova E, Brümmer B, Jørgensen H, Larsen S. On the extension of the wind profile over homogeneous terrain beyond the surface boundary layer. *Bound Layer Meteorol*. 2007;124(2):251-268. https://doi.org/10.1007/s10546-007-9166-9

41. Peña A., Gryning S-E, Hasager C. B.. Measurements and modelling of the wind speed profile in the marine atmospheric boundary layer. *Boundary-Layer Meteorology*. 2008;129(3):479-495. https://doi.org/10.1007/s10546-008-9323-9

42. Obukhov AM. Turbulence in an atmosphere with a non-uniform temperature. *Bound Layer Meteorol*. 1971;2(1):7-29. https://doi.org/10.1007/BF00718085

43. Van Wijk AJM, Beljaars ACM, Holtslag AAM, Turkenburg WC. Evaluation of stability corrections in wind speed profiles over the North Sea. *J Wind Eng Ind Aerodyn*. 1990;33(3):551-566. https://doi.org/10.1016/0167-6105(90)90007-Y

44. Welch P. The use of fast fourier transform for the estimation of power spectra: a method based on time averaging over short, modified periodograms. *IEEE Trans Audio Electroacoustics*. 1967;15(2):70-73. https://doi.org/10.1109/TAU.1967.1161901

45. Veers P. Modeling stochastic wind loads on vertical axis wind turbines. In: 25th Structures, Structural Dynamics and Materials Conference; 1984; Palm Springs,CA,U.S.A.:910.

46. Jørgensen BH, Sørensen JN, Brøns M. Low-dimensional modeling of a driven cavity flow with two free parameters. *Theoret Comput Fluid Dyn*. 2003;16(4):299-317. https://doi.org/10.1007/s00162-002-0082-9

47. Berkooz G, Holmes P, Lumley JL. The proper orthogonal decomposition in the analysis of turbulent flows. *Annual Rev Fluid Mech*. 1993;25(1):539-575. https://doi.org/10.1146/annurev.fl.25.010193.002543

48. Mann J. Wind field simulation. *Probabil Eng Mech*. 1998;13(4):269-282. https://doi.org/10.1016/S0266-8920(97)00036-2

49. Von Kármán Theodore. Progress in the statistical theory of turbulence. *Proc National Acad Sci USA*. 1948;34(11):530-539. https://doi.org/10.1073/pnas.34.11.530

50. Mann J. Atmospheric turbulence. In: Peña A, Hasager CB, Lange J, Anger J, Badger M, Bingöl F, Bischoff O, Cariou J-P, Dunne F, Emeis S, Harris M, Hofsäss M, Karagali I, Laks J, Larsen SE, Mann J, Mikkelsen T, Pao LY, Pitter M, Rettenmeier A, Sathe A, Scanzani F, Schlipf D, Simley E, Slinger C,

Wagner R, Würth I, eds. *Remote Sensing for Wind Energy Wind Energy*. Denmark: DTU Wind Energy; 2013:52–71. http://orbit.dtu.dk/files/55501125/Remote_Sensing_for_Wind_Energy.pdf

51. Chougule A, Mann J, Segalini A, Dellwik E. Spectral tensor parameters for wind turbine load modeling from forested and agricultural landscapes. *Wind Energy*. 2015;18(3):469-481. https://doi.org/10.1002/we.1709

52. De Maré M, Mann J. Validation of the Mann spectral tensor for offshore wind conditions at different atmospheric stabilities. *J Phys Conf Ser*. 2014;524(1):012106. https://doi.org/10.1088/1742-6596/524/1/012106

53. DTU Wind Energy. Pre-processing tools. http://www.hawc2.dk/download/pre-processing-tools. Accessed May 27, 2019; 2018.

54. Nybø A, Nielsen FG, Reuder J. Processing of sonic anemometer measurements for offshore wind turbine applications. *J Phys Conf Ser*. 2019;1356(1):012006. https://doi.org/10.1088/1742-6596/1356/1/012006

55. Rinker JM.. An empirically based stochastic turbulence simulator with temporal coherence for wind energy applications. *Ph.D. Thesis*; 2016.

56. Krogsæter O, Reuder J. Validation of boundary layer parameterization schemes in the weather research and forecasting (wrf) model under the aspect of offshore wind energy applications—part ii: boundary layer height and atmospheric stability. *Wind Energy*. 2015;18(7):1291-1302. https://doi.org/10.1002/we.1765

57. Shaler K, Jonkman J, Doubrawa P, Hamilton N. FAST.Farm response to varying wind inflow techniques. In: AIAA Scitech 2019 Forum; 2019; Golden, CO (United States).

58. Davenport AG. The spectrum of horizontal gustiness near the ground in high winds. *Quart J Royal Meteorol Soc*. 1961;87(372):194-211. https://doi.org/10.1002/qj.49708737208

59. OpenFOAM: The Open Source CFD Toolbox. https://openfoam.org/. Accessed May 28, 2019; 2019.

60. Kristensen L, Jensen NO. Lateral coherence in isotropic turbulence and in the natural wind. *Bound Layer Meteorol*. 1979;17(3):353-373. https://doi.org/10.1007/BF00117924